Supporting Information

Non-halogenated solvent-processed ternary-blend solar cells via alkyl-side-chain engineering of a non-fullerene acceptor and their application in large-area devices

Taeho Lee,[‡a] Sora Oh,[‡bc] Shafket Rasool,[bc] Chang Eun Song,[*bc] Dongwook Kim,[a] Sang Kyu Lee,[bc] Won Suk Shin,[*bcd] and Eunhee Lim[*a]

[a] Department of Chemistry, Kyonggi University, 154-42 Gwanggyosan-ro, Yeongtong-gu, Suwon 16227, Republic of Korea, E-mail: ehlim@kyonggi.ac.kr

[b] Energy Materials Research Center, Korea Research Institute of Chemical Technology (KRICT), 141 Gajeong-ro, Yuseong-gu, Daejeon 34114, Republic of Korea, E-mail: songce@krict.re.kr, shinws@krict.re.kr

[c] Advanced Materials and Chemical Engineering, University of Science and Technology (UST), 217 Gajeong-ro, Yuseong-gu, Daejeon 34113, Republic of Korea

[d] KU-KRICT Collaborative Research Center & Division of Display and Semiconductor Physics & Department of Advanced Materials Chemistry, Korea University, 2511 Sejong-ro, Sejong 30019, Republic of Korea

[‡] T. L. and S. O. contributed equally to this work.

*Corresponding authors. E-mail: songce@krict.re.kr (C. E. Song), shinws@krict.re.kr (W. S. Shin), and ehlim@kyonggi.ac.kr (E. Lim)

Contents

1. Experimental Section

Nuclear magnetic resonance (NMR): The ^{13}C NMR spectrum of **T2-OEHRH** was analyzed on a Bruker AVANCE III 500 (Bruker, Germany) installed at the National Center for Inter-university Research Facilities (NCIRF) at Seoul National University. All other ^{1}H and ^{13}C NMR spectra were recorded on a Bruker AVANCE III HD400 (Bruker, Germany).

Solubility measurement method: The solubility of each compound in chloroform (CF) or toluene was determined as follows: A supersaturated solution of each compound was stirred for 48 hours at room temperature then allowed to stand still for 12 hours. The slurry was then filtered through a 0.45 μm PTFE filter. The filtrates solution is concentrated and then measured the quantity. The solubility measurement method considered in the related literatures.[S1]

DFT calculations: Non-fullerene acceptor (NFA) derivatives and their constituting subunits, *i.e.*, backbone and side chains were calculated using ωB97X-D functional and 6-31G(d) basis sets. All the computed structures were confirmed to be in local minima by conducting additional harmonic frequency calculations. Dimer structures of NFA derivatives were optimized for the syn- and anti-conformations. Interactions between the backbones and those between side chains were assessed at the optimized dimer structures. Interactions between backbone of one molecule and side chains of the other were omitted for the sake of simplicity. All these calculations were carried out with Gaussian 16 program package revision B.01.[S2]

UV-vis absorption: UV-vis absorption spectra were recorded using a Shimadzu UV-36000 spectrophotometer with solution in CF and a thin film on a quartz substrate.

Mass spectroscopy (MS): High resolution mass spectrometry (HRMS) was performed on JMS-700 (JEOL, Japan).

Elemental analysis (EA): Elemental analysis was performed on solid samples using a Vario-Micro Cube elemental analyzer at the Korean Basic Science Institute (KBSI) Pusan Center.

Thermogravimetric (TGA): Thermogravimetric analysis (TGA) was performed using a TGA/DSC 1 (Mettler-Toledo, Switzerland) under a N_2 atmosphere at a heating rate of 10 ℃ min^{-1}.

Differential scanning calorimetry (DSC): Differential scanning calorimetry (DSC) was performed using a DSC 1 (Mettler-Toledo, Switzerland) under a N_2 atmosphere at a heating or cooling rate of 10 ℃ min^{-1}.

Cylic voltammetry (CV): The electrochemical properties of the NFAs were studied by cyclic voltammetry (CV) with a BAS 100B electrochemical analyzer. A three-electrode system was used and consisted of a non-aqueous reference electrode (0.1 M Ag/Ag^+ acetonitrile solution), a platinum working electrode, and a platinum wire as a counter electrode. The redox potential of the NFAs was measured in acetonitrile with 0.1 M (n-$C_4H_9)_4N$-PF_6 at a scan rate of 100 mV/s. The films were prepared by dip-coating the NFA solution onto the platinum working electrode, and the measurements were calibrated using the ferrocenium/ferrocene redox value of –4.8 eV as an external reference. The highest occupied molecular orbital (HOMO) and lowest unoccupied molecular orbital (LUMO) energy levels were estimated according to the empirical relationship $E_{HOMO} = –(E_{onset,ox} – E_{1/2,ferrocene} + 4.8)$ eV and $E_{LUMO} = –(E_{onset,red} – E_{1/2,ferrocene} + 4.8)$ eV, where $E_{onset,ox}$ and $E_{onset,red}$ are the onset potentials of oxidation and

reduction, respectively, assuming that the energy level of ferrocene (Fc) is 4.8 eV below the vacuum level.[S3-S4]

Atomic Force Microscopy (AFM): AFM specimens were prepared by using the same procedures with optimal conditions but without the MoO_x/Ag top electrode.

Transition Electron Microscopy (TEM): TEM specimens were prepared casting the ternary-blend films with optimum conditions on an ITO/PEDOT:PSS substrate, and then floating the film on the water surface, and finally transferring into TEM grids. The TEM images were taken on JEOL JEM-2200FS.

Hole and Electron-Only Devices Fabrication and Mobility Measurement: Charge carrier mobilities were measured using the SCLC method, which is described by $J = 9\varepsilon_0\varepsilon_r\mu V^2/8L^3$. Here, J is the current density, L is the ternary-blend film thickness, μ is the hole or electron mobility, ε_r is the relative dielectric constant of the transport medium, ε_0 is the permittivity of free space (8.85×10^{-12} Fm^{-1}), V is the internal voltage in the device and $V = V_{appl} - V_{bi} - V_r$, where V_{appl} is the applied voltage to the device, V_{bi} is the built-in voltage due to the relative work function difference between the two electrodes and V_r is the voltage drop due to contact resistance and series resistance across the electrodes. Hole-only devices were fabricated with a structure of ITO/PEDOT:PSS/ternary-blend films/Au. Meanwhile, electron-only devices were fabricated with a structure of ITO/ZnO NPs/PEIE/ternary-blend films/Ca/Al.

2D-GIWAXS Analysis: The GIWAXS measurements were conducted at PLS-II 3C beamline of Pohang Acceleartor Laboratory (PAL) in Republic of Korea. The GIWAXS samples were spin-cast onto the Si/ZnO/PEIE substrate. GIWAXS data were recorded. All GIWAXS patterns

were recorded with a 2D CCD detector and the X-ray irradiation time was 2 ~ 120 seconds dependent on the saturation level of the detector at a range of grazing angles between θ = 0.12 ° and 0.18 °. Diffraction angles were calibrated by a pre-calibrated sucrose and the sample-to-detector distance was about 223.2 mm. All the GIWAXS images have been processed using customised MATLAB software that was developed in-house.

IMPS and IMVS Analysis: All IMPS and IMVS methods were performed using an IviumStat instrument (Ivium Technologies) equipped with a four-wire impedance test interface (in a two-probe configuration). Both the DC and AC components of the illumination were provided by a red-emitting LED (λ = 635 nm, V_{appl} = 1.5V) as the light source for this study. IMPS and IMVS were measured over a range of 5×10^5 Hz to 8×10^5 Hz under short-circuit conditions and over a range of 3×10^3 Hz to 1×10^5 Hz under open-circuit conditions, respectively. For IMPS and IMVS measurements, a red LED was modulated to a depth of ca. 2% using a Stanford lock-in-amplifier (SR810) and purpose built LED driver with an adjustable DC offset. All experiments were performed in an earthed Faraday dark-box to eliminate electrical noise. Photocurrents were measured using a battery powered current preamplifier (Stanford SR570) and photovoltages measured using a purpose built battery powered high impedance voltage follower (input impedance 1012 Ω). The phase and amplitude of the resultant AC photocurrent (or photovoltage) were captured using the lock--in amplifier (SR810) under computer control (Labview).[S5]

NEXAFS Analysis: NEXAFS measurements were performed at the PLS-II 4D PES beamline of PAL in Repulic of Korea. We used the total electron yield (TEY) detection mode for the NEXAFS spectra by recording the sample current normalized to a signal current, which was measured simultaneously using a gold mesh under ultrahigh vacuum ($<10^{-9}$ Torr). In this case,

a *p*-polarized (≈85%) synchrotron photon beam had an energy in a range of 270–325 eV and a spectral energy resolution of ΔE = 150 meV. In particular, NEXAFS can measure the average orientation of the π-conjugated planes in organic semiconductors by collecting carbon K-edge spectra obtained from various angles of incidence of the synchrotron photon beam from the surface plane. Furthermore, detailed structural information, such as the tilting angle of the conjugated planes, can be derived from the spectra. The features in the NEXAFS spectra are assigned to the π* (C=C) orbital at 285.4 eV. To determine the tilt angle (α) between the C=C double bond in the conjugated planes and the Si/ZnO NPs/PEIE substrate surface, a fourfold symmetry of the substrate was used with the photon beam, which had a beam size of 0.1 × 0.3 mm^2. The peak intensities of the π* (C=C) orbital in the NEXAFS spectra were then fitted by the following Equation S1

$$I_v \propto \left[\frac{P}{3}\left\{1+\frac{1}{2}(3cos^2\theta-1)(3cos^2\alpha-1)\right\}+\frac{(1-P)}{2}sin^2\alpha\right] \qquad \text{(S1)}$$

where θ is the polarization angle of the incident synchrotron light with respect to the normal to the surface, and P = 0.85 is used for the degree of polarization. In addition, the dichroic ratio (*R*), which represents the average chain conformation of films, was calculated using Equation S2

$$R = \frac{/(90°)-/(0°)}{/(90°)+/(0°)} \qquad \text{(S2)}$$

which is the difference between the intensities at θ = 90° and 0°, divided by their sum. The value of *R* varies from +0.7 (for horizontal π* orbital and α = 90°), to 0 (for random orientation, known as magic angle α = 54.7°) and −1 (for a vertical π* orbital and α = 0°): a more positive *R* signifies a larger average tilting angle of the transition dipole away from the substrate.

Small-area OSCs Fabrication: The device structure was ITO/ZnO/PEIE/ternary-blend photoactive films/MoO_x/Ag. The pre-patterned ITO glass substrates were ultrasonicated in deionized water with detergent, acetone, and isopropanol, sequentially. After being dried at 140 ^oC in an oven for 3 hours, the substrates were further treated by UV-ozone exposure for 20 min. A thin layer (30 nm) of ZnO NPs in butanol (10 mg mL^{-1}) was deposited at 3000 rpm for 40s, and then baked at 100 ℃ for 10 min. The polyethylenimine, 80% ethoxylated (PEIE) solution was prepared by dissolving PEIE in ethanol at a weight concentration of 0.1 wt%. The PEIE layer (5 nm) was deposited onto the ZnO NPs at 4000 rpm for 60 s and then annealed immediately at 100 ℃, for 10 min. The ITO/ZnO NPs/PEIE substrates were subsquently transferred to the nitrogen-filled glovebox for deposition of the photoactive layer. The PTB7-Th:EH-IDTBR:NFA (1.0:1.0:1.0, w/w) solutions were spin-cast on top of the PEIE layer at 2000 rpm for 30 seconds. Finally, MoO_x (10 nm) and Ag (100 nm) were deposited on the top of the ternary-blend photoactive layer in a high vacuum chamber (~10^{-6} Torr). The photovoltaic properties of small-area OSCs were evaluated through a photomask with an aperture size of 0.09 cm^2.

Large-area OSCs Module Fabrication: For the large-area device (aperture size = 55.5 cm^2), the ZnO NPs (30 nm), PEIE (5 nm) and ternary-blend photoactive layer were coated onto UV-ozone-treated ITO/glass substrate (100 cm^2) using a D-bar coater manufactured by PEMS (Republic of Korea). The D-bar speed was kept at 7 mm/sec for the depositon of both the ZnO NPs and PEIE layer. For the coating of the photoactive solutions, the D-bar speed was kept at 15 mm/sec and 20 uL of PTB7-Th:EH-IDTBR:**T2-OEHRH** (1.0:1.0:1.0, w/w) solution with 1.0 vol% DPE. Finally, 10nm of MoO_x and 100 nm of Ag were thermally evaporated to complete the module in a vacuum chamber with a base pressure of 1×10^{-6} Torr.

Efficiency and External Quantum Efficiency (EQE) of OSCs: OSCs efficiencies were characterized from *J-V* curve measurements using a Keithley 2400 sourcemeter and a solar simulator (K201 LAB55, McScience), under simulated 100 mW cm^{-2} irradiation from a Xe arc lamp with an AM 1.5G filter. Simulator irradiance was characterized using a calibrated spectrometer, and the illumination intensity was set using an NREL-certified silicon diode with an integrated KG1 optical filter. EQEs were measured using a spectral measurement system (K3100 IQX, McScience Inc.), which applied monochromatic light from a 100 W Xe arc lamp filtered by an optical chopper and a monochromator.

2. NMR spectra

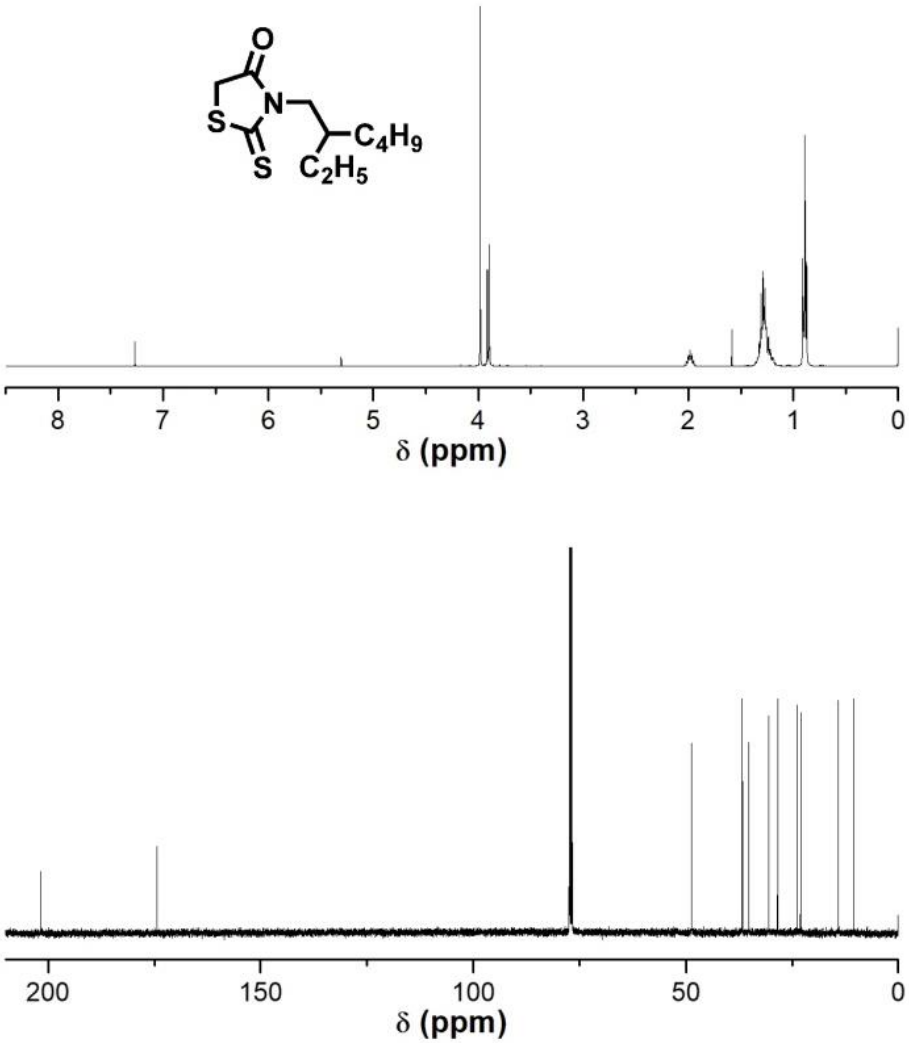

Figure S1. ^{1}H (top) and ^{13}C (bottom) NMR spectra of EHRH.

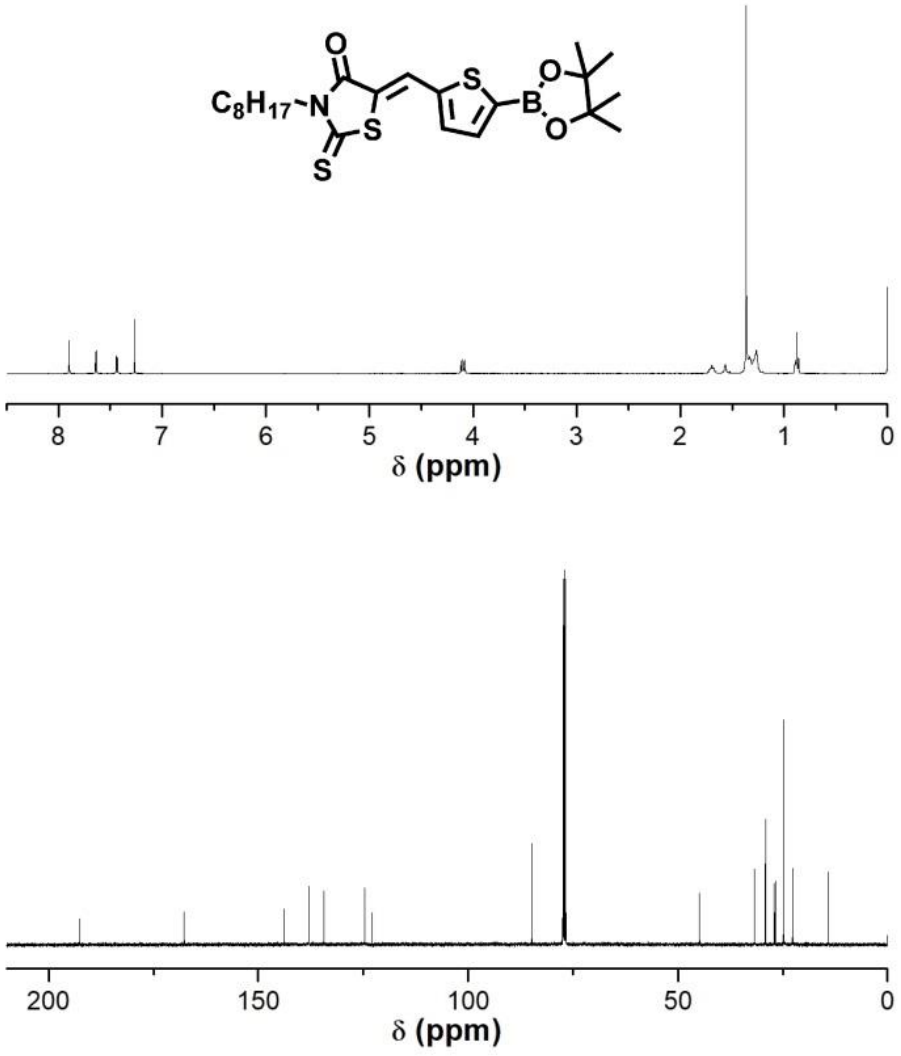

Figure S2. ^{1}H (top) and ^{13}C (bottom) NMR spectra of compound **1**.

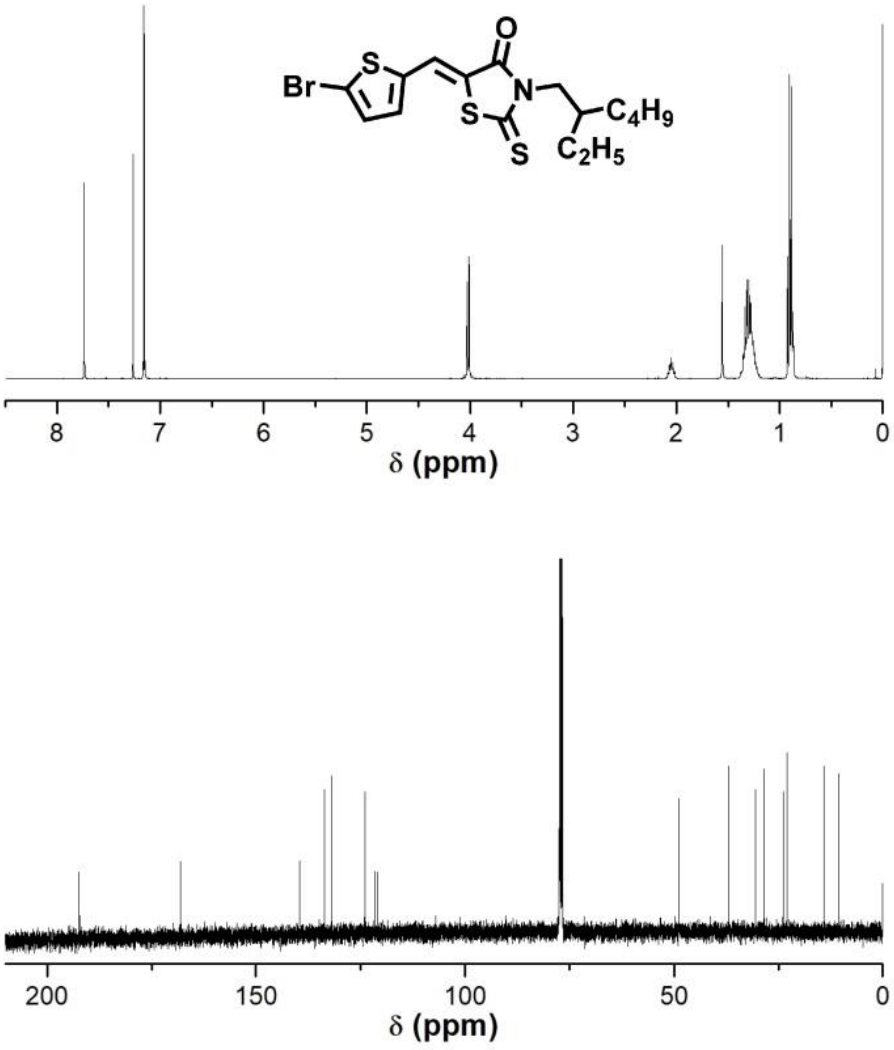

Figure S3. ^{1}H (top) and ^{13}C (bottom) NMR spectra of compound **2**.

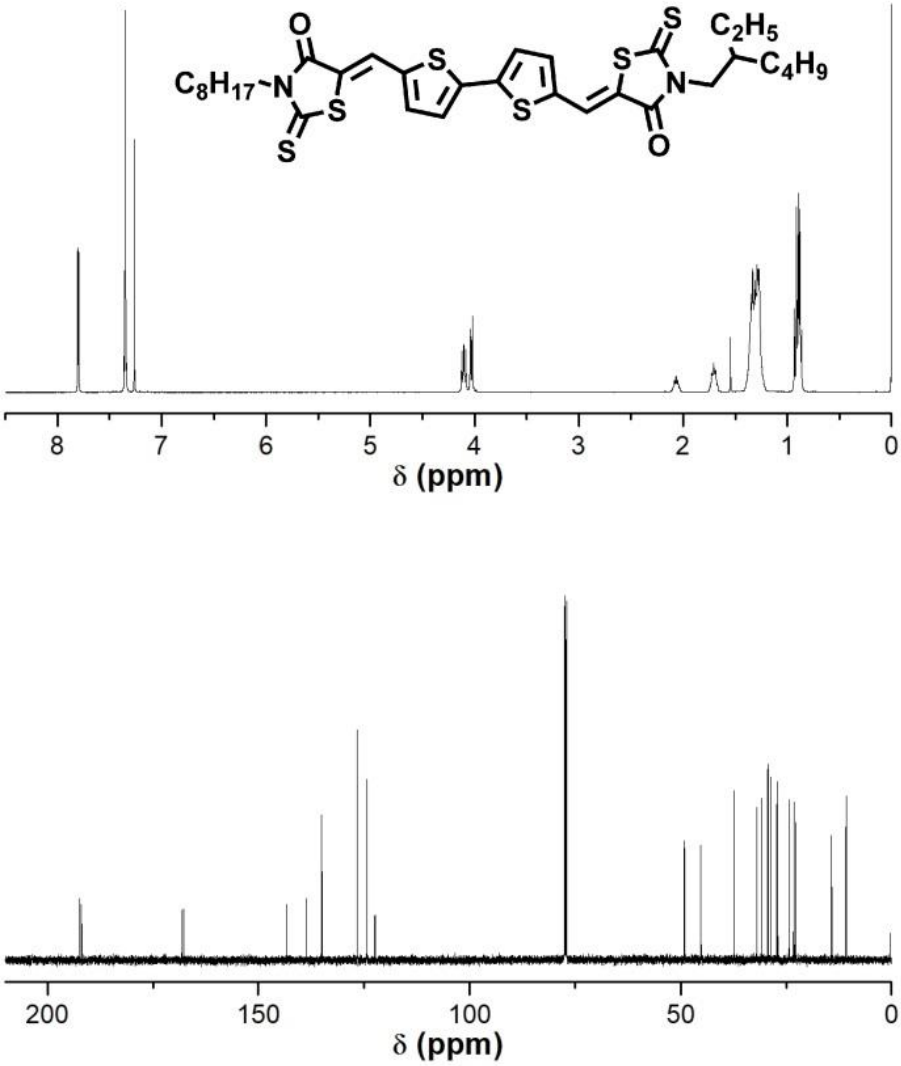

Figure S4. ^{1}H (top) and ^{13}C (bottom) NMR spectra of **T2-OEHRH**.

3. Additional Figures and Tables

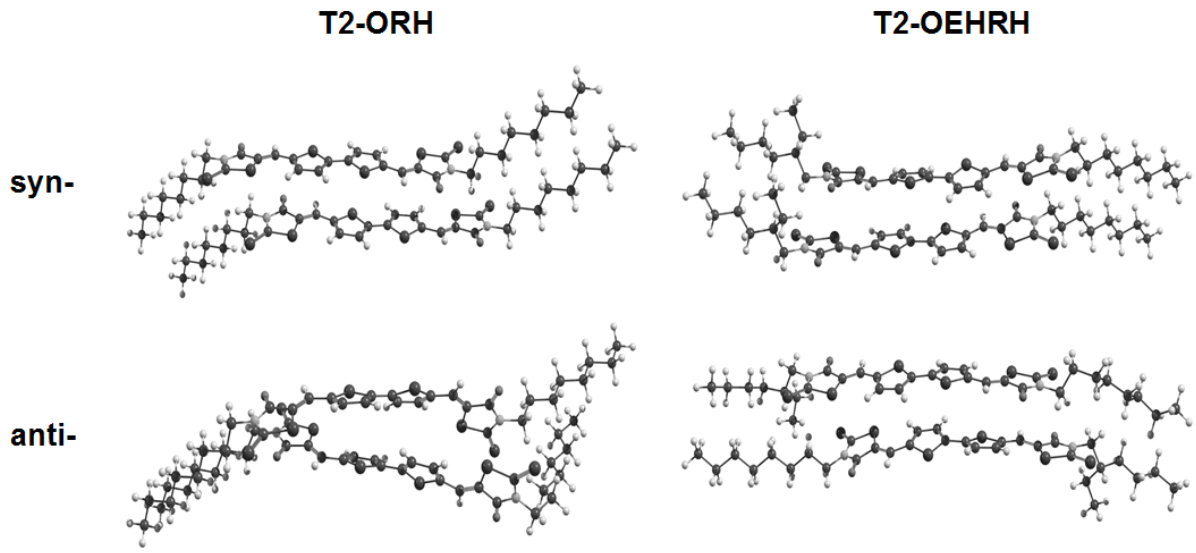

Figure S5. Illustration of representative optimized dimer structures of NFA derivatives.

Table S1. Calculated intermolecular interactions (in eV) between NFA derivatives in the syn and anti conformer.

	T2-ORH			T2-OEHRH		
	Total	**Backbone**	**Side chains**	**Total**	**Backbone**	**Side chains**
Syn	-1.81	-0.89	-0.24/-0.24	-1.57	-0.89	-0.22/-0.18
Anti	-1.74	-0.84	-0.31/-0.21	-1.53	-0.83	-0.25/-0.08

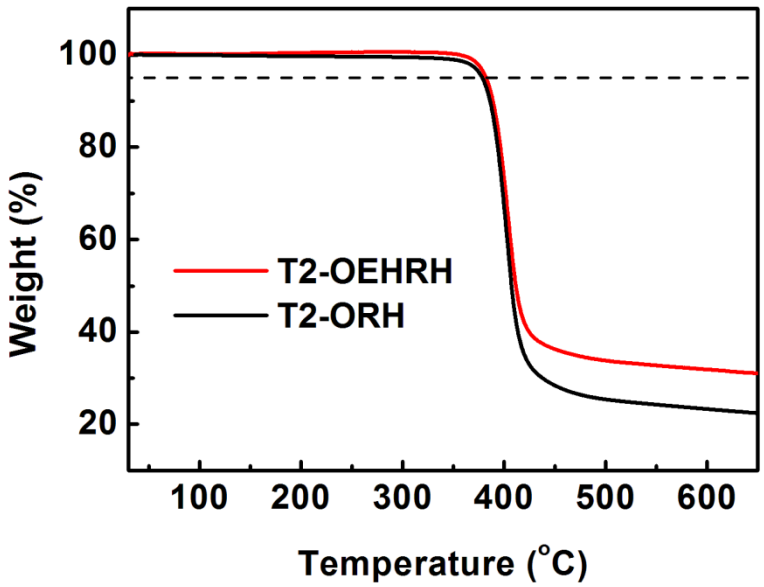

Figure S6. TGA curves of of NFAs.

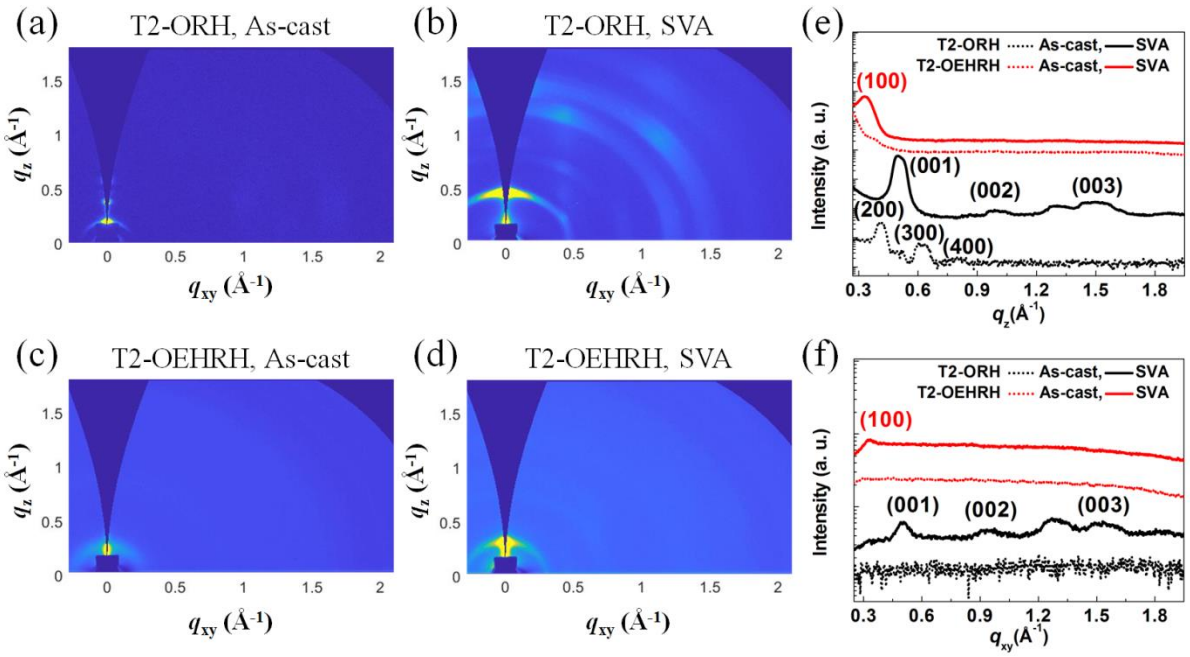

Figure S7. 2D-GIWAXS patterns for (a) as-cast, (b) SVA-treated **T2-ORH** and (c) as-cast, (d) SVA-treated **T2-OEHRH**. (e) Out-of-plane and (f) in-plane line-cut profiles from the 2D-GIWAXS patterns of NFAs.

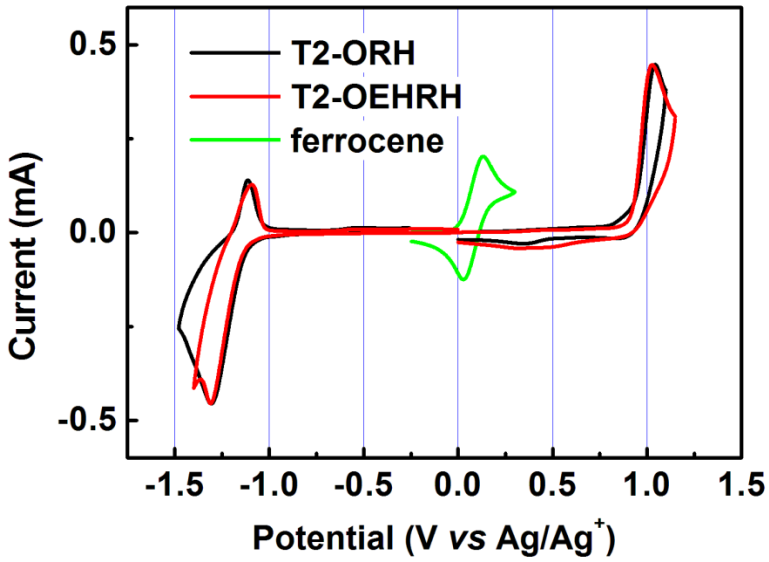

Figure S8. Cyclic voltammograms of NFAs.

Table S2. Photovoltaic parameters of ternary-blend NFA-OSCs (PTB7-Th:NFAs = 1.0:2.0) with different EH-IDTBR:**T2-OEHRH** weight ratios under simulated 1 sun (100 mW cm^{-2}, AM 1.5G) irradiation[a,b]

NFAs (EH-IDTBR:T2-OEHRH)	V_{OC} [V]	J_{SC} [mA/cm^2]	*FF* [%]	PCE [%]
1.3:0.7	1.03 (1.04 ± 0.01)	17.54 (17.41 ± 0.13)	61 (60 ± 1)	11.05 (10.79 ± 0.26)
1.0:1.0	1.04 (1.04 ± 0.01)	18.05 (17.90 ± 0.14)	65 (64 ±1)	12.10 (11.89 ± 0.21)
0.7:1.3	1.04 (1.03 ± 0.01)	17.80 (17.68 ± 0.12)	62 (61 ± 1)	11.50 (11.34 ± 0.17)

[a] Inverted device architecture is ITO/ZnO NPs/PEIE/PTB7-Th:NFAs (1.0:2.0, *d* = ~100nm)/MoO_x/Ag. [b] The average values with standard deviations in the brackets are obtained from over 10 independent devices.

Table S3. Summary of photovoltaic parameters based on ternary-blend NFA-OSCs (EH-IDTBR:**T2-OEHRH** = 1.0:1.0) with different PTB7-Th:NFAs (D:A) weight ratios under simulated 1 sun (100 mW cm^{-2}, AM 1.5G) irradiation[a,b]

D:A [w/w]	V_{OC} [V]	J_{SC} [mA/cm^2]	*FF* [%]	PCE [%]
1.0:1.0	1.04 (1.04 ± 0.01)	15.97 (15.87 ± 0.11)	57 (56 ± 1)	9.51 (9.38 ± 0.14)
1.0:2.0	1.04 (1.04 ± 0.01)	18.05 (17.90 ± 0.14)	65 (64 ± 1)	12.10 (11.89 ± 0.21)
1.0:3.0	1.04 (1.04 ± 0.01)	17.59 (17.42 ± 0.16)	63 (63 ± 1)	11.55 (11.32 ± 0.24)

[a] Inverted device architecture is ITO/ZnO NPs/PEIE/PTB7-Th:NFAs (*d* = ~100 nm)/MoO_x/Ag. [b] The average values with standard deviations in the brackets are obtained from over 10 independent devices.

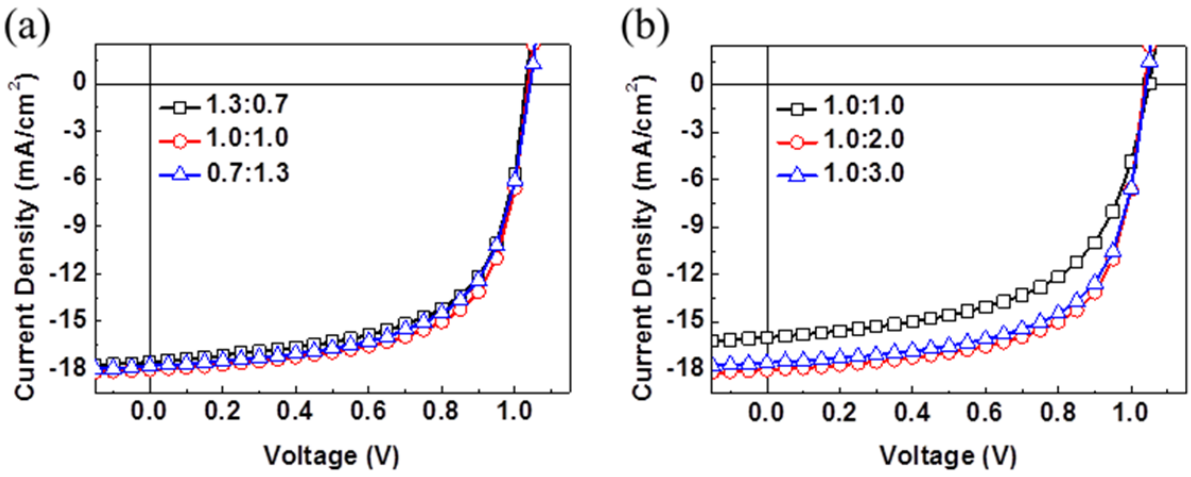

Fig S9. (a) *J*–*V* characteristics of ternary-blend OSCs with different EH-IDTBR:**T2-OEHRH** blend ratios under AM 1.5G illumination with a light intensity of 100 mW cm^{-2}. (b) *J*–*V* characteristics of ternary-blend OSCs with different D:A (PTB7-Th:NFAs) blend ratios under AM 1.5G illumination with a light intensity of 100 mW cm^{-2}.

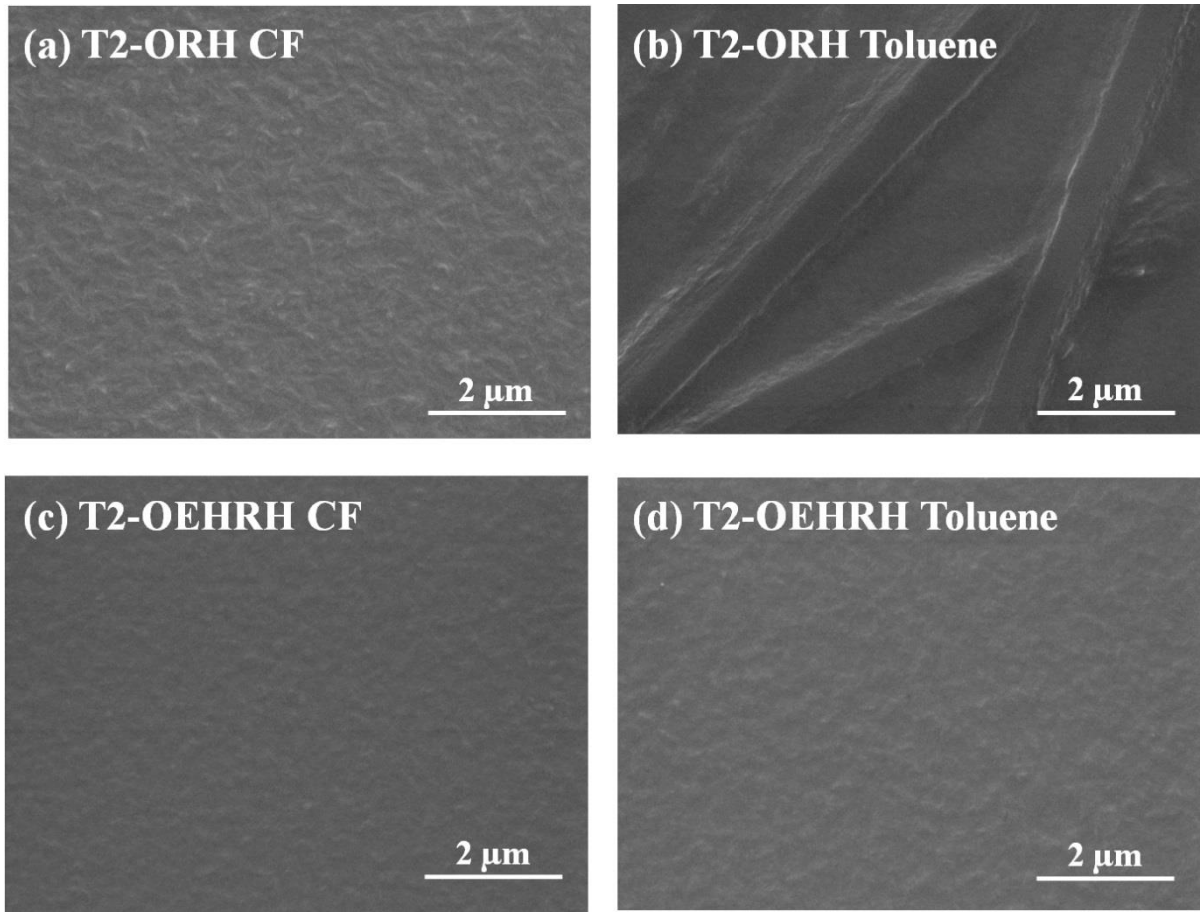

Figure S10. Higher-magnification SEM images of PTB7-Th:EH-IDTBR:**T2-ORH** with (a) CF solvent and with (b) toluene solvent, (c) PTB7-Th:EH-IDTBR:**T2-OEHRH** with (c) CF solvent and with (d) toluene solvent.

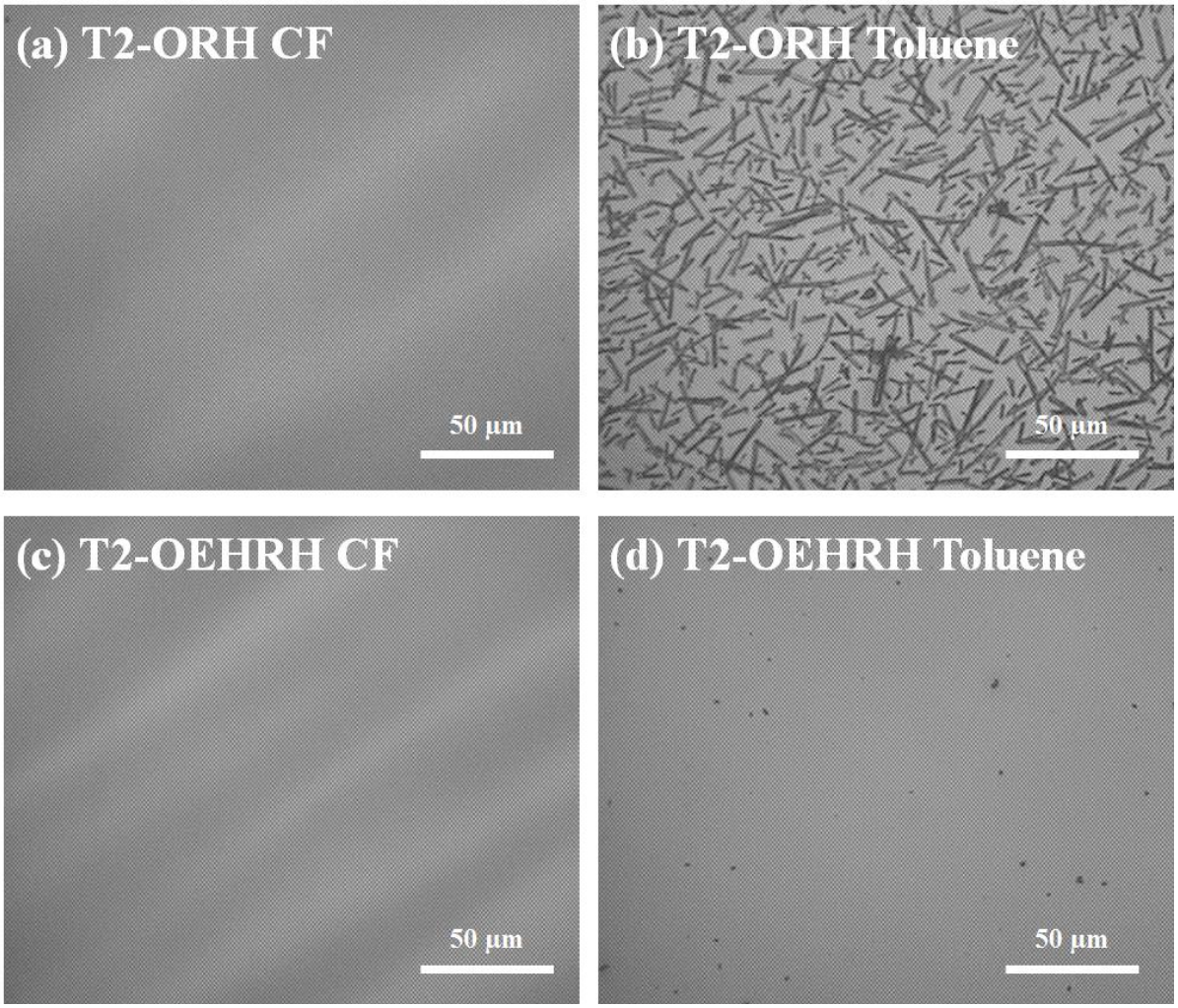

Figure S11 Optical microscopy images of PTB7-Th:EH-IDTBR:**T2-ORH** with (a) CF solvent and with (b) toluene solvent, (c) PTB7-Th:EH-IDTBR:**T2-OEHRH** with (c) CF solvent and with (d) toluene solvent.

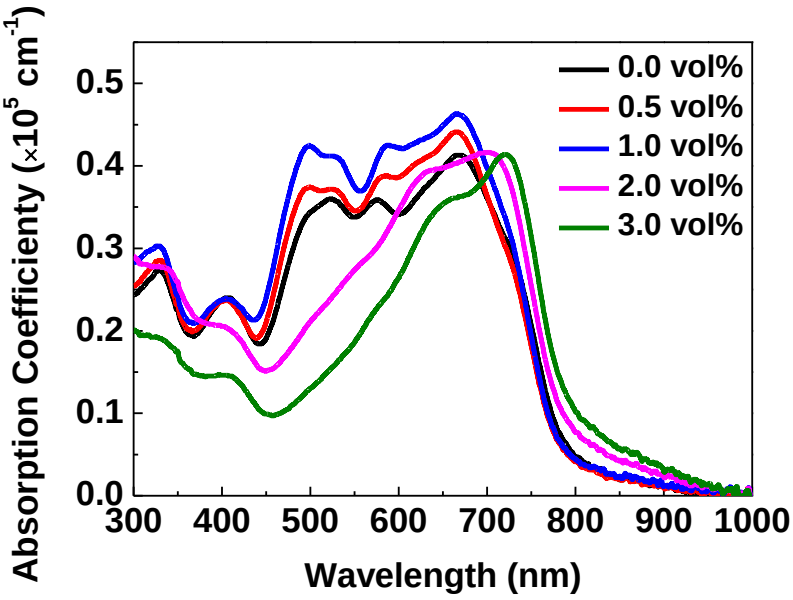

Figure S12 Normalized absorption coefficienty of ternary-blend photoactive films processed from different DPE additive volumes.

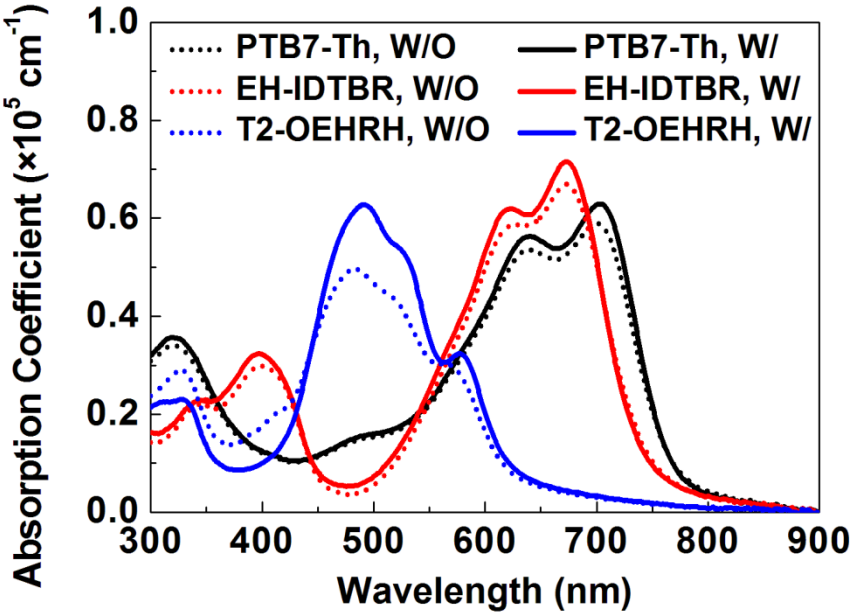

Figure S13 UV-vis absorption coefficient of neat PTB7-Th, EH-IDTBR, and **T2-OEHRH** without and with 1.0 vol% DPE additive.

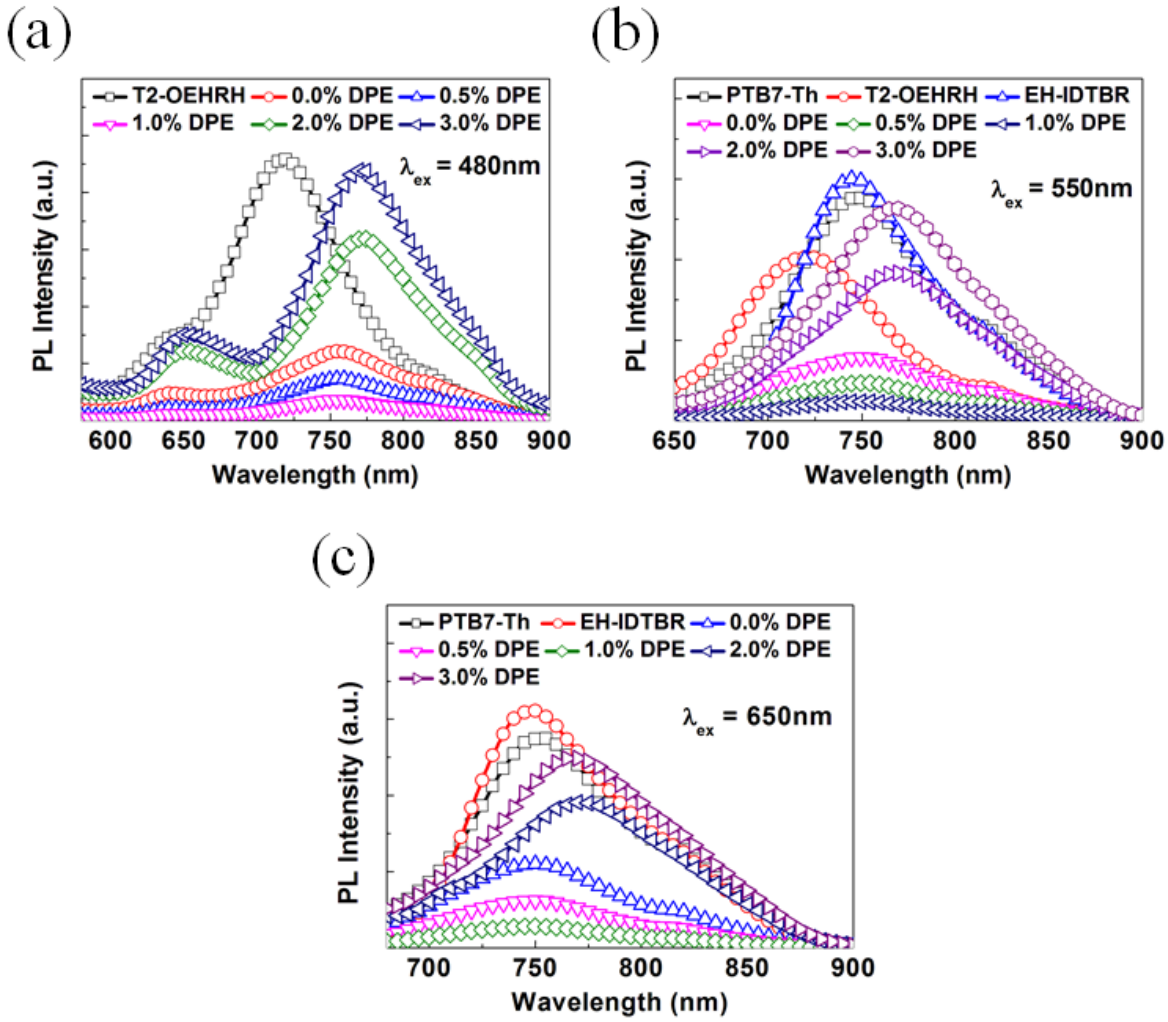

Figure S14. The PL spectra of neat photoactive components and ternary-blend photoactive films with different DPE fractions and each PL spectrum was measured under different excitation wavelengths: (a) 480 nm, (b) 550 nm, and (c) 650 nm.

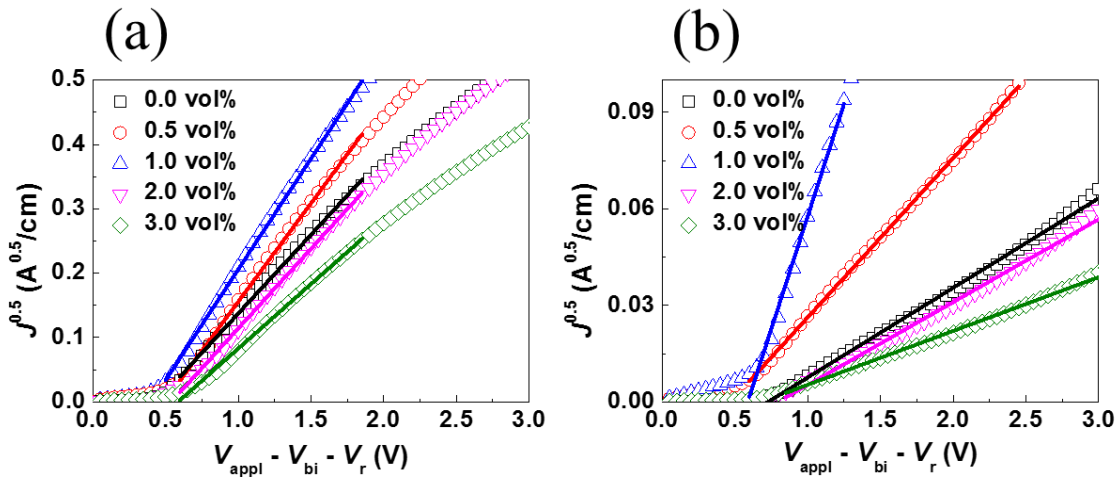

Figure S15. Dark *J*-*V* characteristics from the (a) hole-only and (b) electron-only devices.

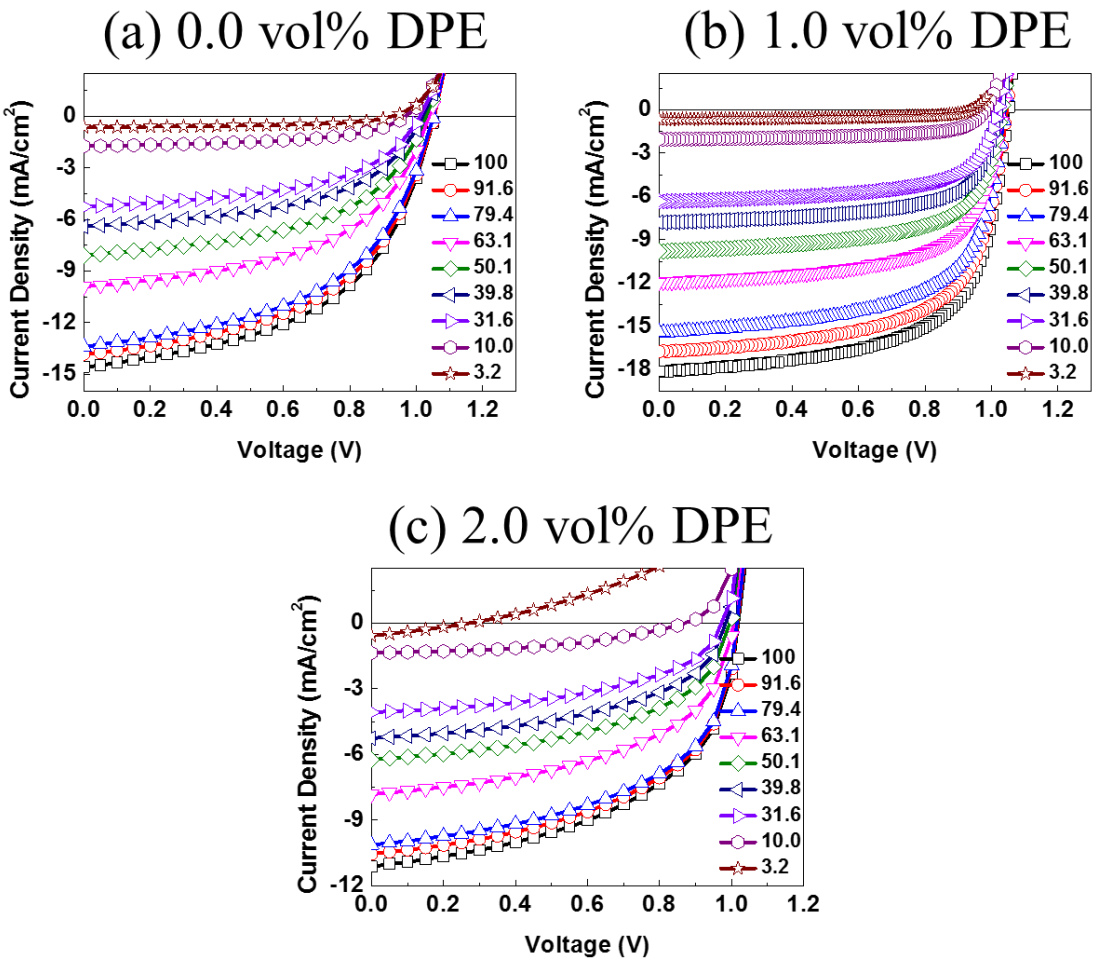

Figure S16. Light intensity-dependent *J*-*V* curves in ternary-blend NFA-OSCs with the (a) 0.0 vol%, (b) 1.0 vol%, and (c) 2.0 vol% DPE additive.

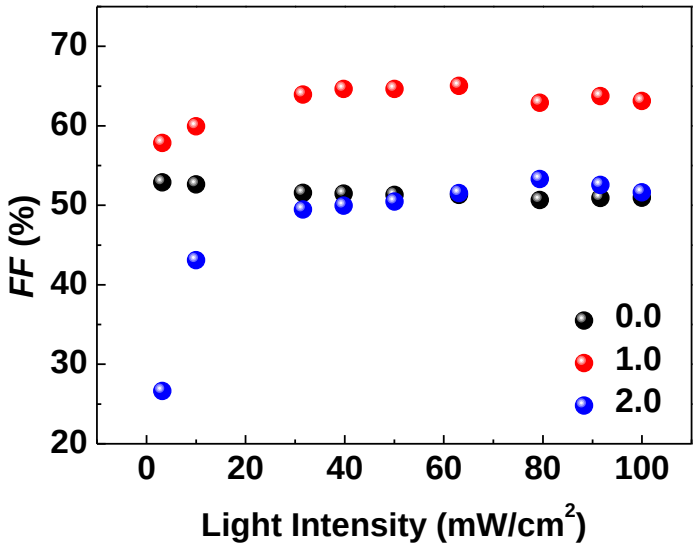

Figure S17. Measured *FF* of the ternary-blend NFA-OSCs with different vol% DPE additive against light intensity.

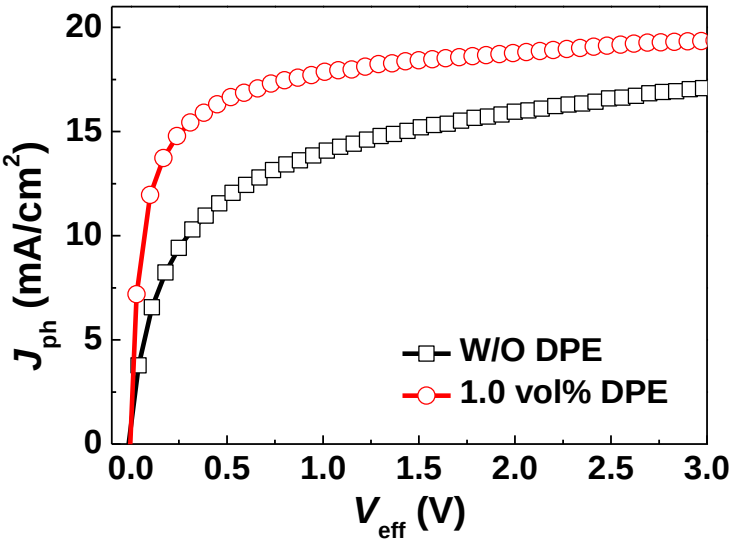

Figure S18. Photocurrent density dependence on the effective voltage of ternary-blend NFA-OSCs without and with 1.0 vol% DPE additive.

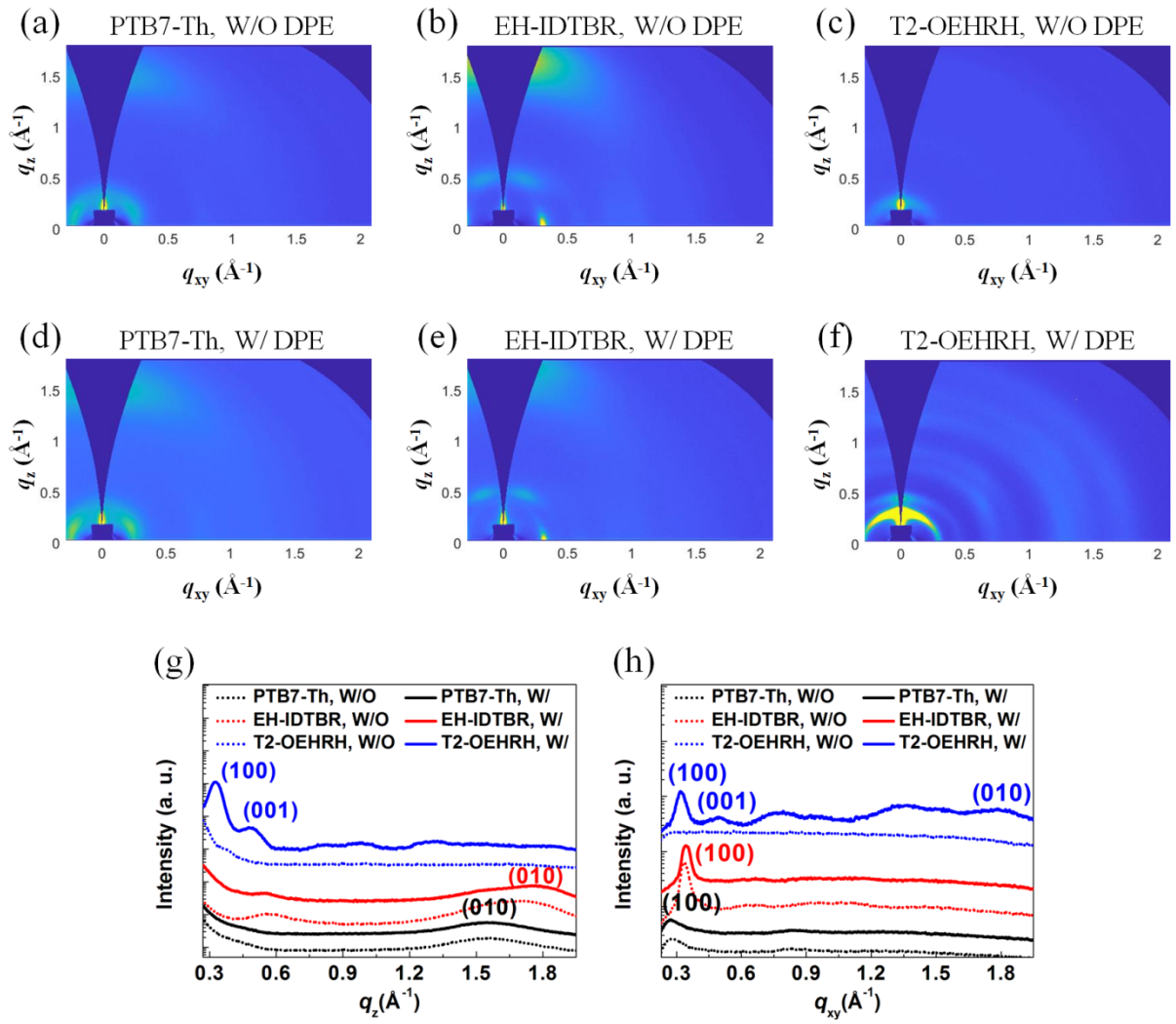

Figure S19. 2D-GIWAXS patterns of neat PTB7-Th (a) without and (d) with 1.0 vol% DPE, neat EH-IDTBR (b) without and (e) with 1.0 vol% DPE, and neat **T2-OEHRH** (c) without and (f) with 1.0 vol% DPE. One-dimensional integrated scattering profiles for the corresponding neat films in the (g) out-of-plane and (h) in-plane directions.

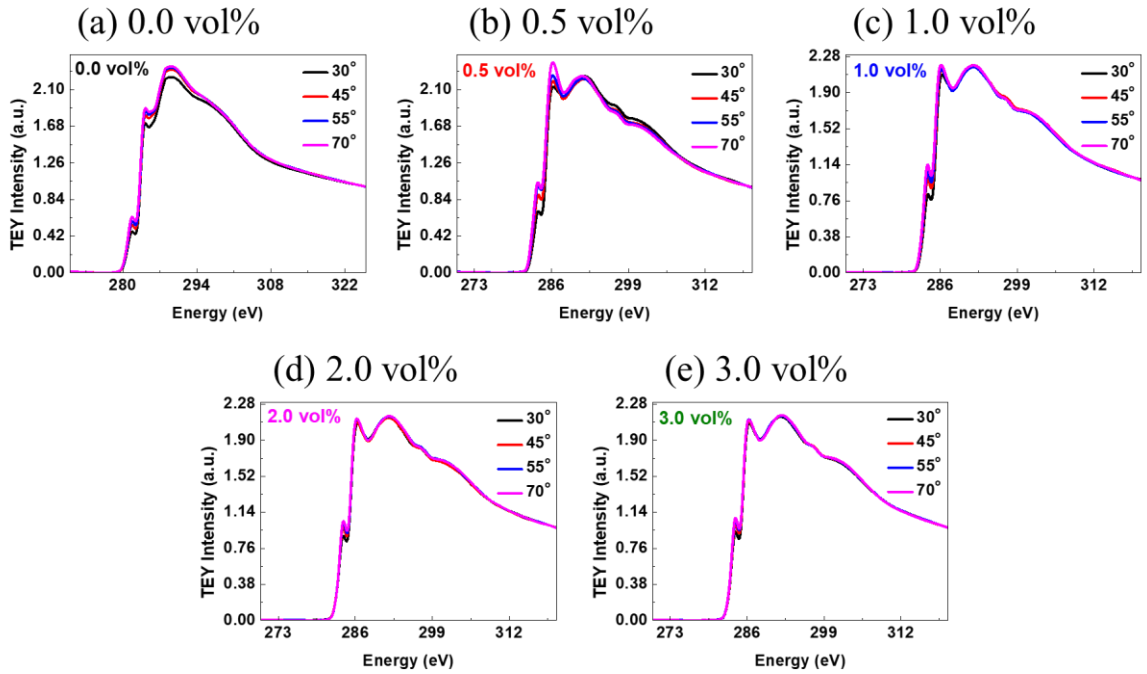

Figure S20. NEXAFS TEY mode of PTB7-TH:EH-IDTBR:**T2-OEHRH** (1:1:1) with different DPE additive for (a) 0.0 vol%, (b) 0.5 vol%, (c) 1.0 vol%, (d) 2.0 vol%, and (e) 3.0 vol% at different incidence angles.

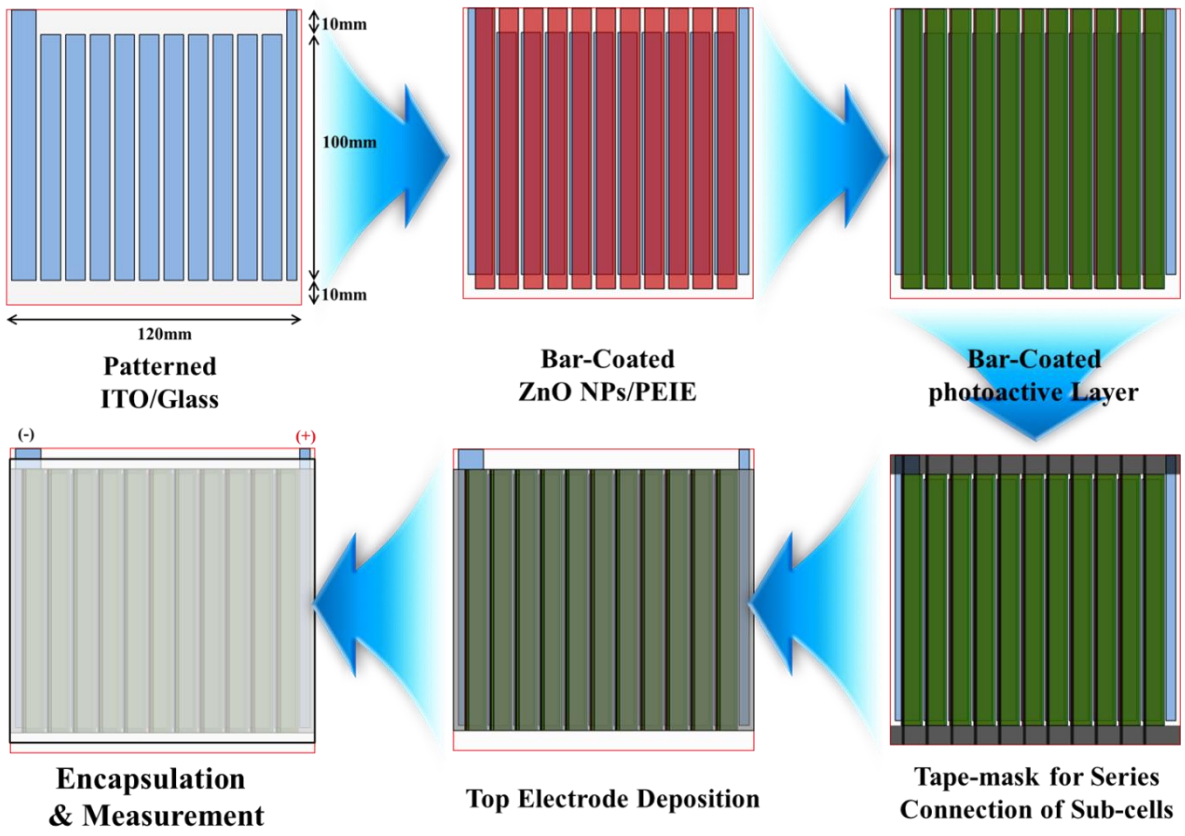

Figure S21. Schematic diagram for preparing sub-module ternary-blend OSCs based on **T2-OEHRH** processed from non-halogenated solvent systems using the D-bar coating in air.

4. Literature survey for large-area high-efficiency OSC modules

Table S4. PCEs of large-area OSC modules processed from non-halogenated solvents.

Photoactive layer	Photoactive area (cm^2)	Processing solvent[a]	PCE (%)
Fullerene-based acceptors			
POD2T-DTBT:$PC_{71}BM$	24	*o*-XY:salicylaldehyde	3.93 [S6]
PBTZT-*stat*-BDTT-8:$PC_{61}BM$	98	XY:tetralin	3.95 [S7]
PBDTTT-CT:$PC_{71}BM$	10.8	toluene	4.2 [S8]
PNTz4T:$PC_{71}BM$	54.45	XY	4.29 [S9]
PBTZT-*stat*-BDTT-8:$PC_{61}BM$	68.76	XY:tetralin	4.3 [S10]
PBTZT-*stat*-BDTT-8:$PC_{61}BM$	114.5	XY:tetralin	4.5 [S11]
PBTZT-*stat*-BDTT-8:$PC_{61}BM$	197.40	XY:tetralin	4.8 [S10]
PTB7-Th:*p*-DTS$(FBTTH_2)_2$:$PC_{71}BM$	20	XY	5.18 [S12]
PBTZT-*stat*-BDTT-8:$PC_{61}BM$	35	XY:tetralin	5.28 [S7]
PTB7-Th:*p*-DTS$(FBTTH_2)_2$:$PC_{71}BM$	10	XY	5.82 [S12]
PNTz4T-5MTC:$PC_{71}BM$	54.45	XY	6.61 [S9]
PTB7-Th:$PC_{71}BM$	16	*o*-methylanisole	7.5 [S13]
PV2000:$PC_{71}BM$	23.7	*o*-XY	7.56 [S14]
Non-Fullerene-based acceptors			
P3HT:O-IDTBR	59.92	*o*-methylanisole	4.7 [S15]
PTB7-Th:**T2-OEHRH**:EH-IDTBR	55.5	toluene	9.32 (**this work**)

[a] XY = xylene, tetralin = 1,2,3,4-tetrahydronaphthalene

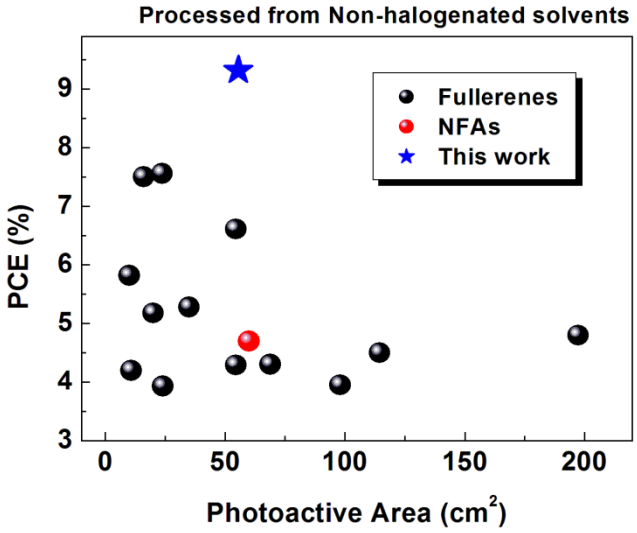

Figure S22. PCE vs photoactive area for large-area OSC modules processed from non-halogenated solvents.

Table S5. PCEs of large-area OSC modules processed from halogenated solvents.

Photoactive layer	Photoactive area (cm^2)	Processing solvent[a]	PCE (%)
Fullerene-based acceptors			
P3HT:$PC_{61}BM$	30	DCB	1.8 [S16]
P3HT:ICBA	57	DCB	1.81 [S17]
P3HT:$PC_{71}BM$	108	CB	2.66 [S18]
PCDTBT: $PC_{71}BM$	25	DCB	3.17 [S19]
P3HT: $PC_{61}BM$	57	DCB	3.39 [S17]
POD2T-DTBT: $PC_{71}BM$	108	CB	3.64 [S18]
PBDTTT-C:$PC_{71}BM$	50.4	CB	5.4 [S20]
PDTT-BOBT:$PC_{71}BM$	66.7	CB	5.44 [S21]
PTB7-Th:$PC_{71}BM$	216	CB	5.63 [S22]
PTB7-Th:$PC_{71}BM$	10.8	CB	5.9 [S8]
D5A:$PC_{71}BM$	62.7	CB	6.54 [S23]
PTB7-Th:$PC_{71}BM$	16.6	CB	7.4 [S24]
BDT2:$PC_{71}BM$	77.8	CF	7.45 [S25]
PBDB-T:$PC_{71}BM$	15	CB	7.58 [S30]
PBDB-T:ITIC:$PC_{71}BM$	216	CB	7.69 [S26]
PTB7-Th:COi8DFIC:$PC_{71}BM$	30	CB	8.6 [S29]
Non-Fullerene-based acceptors			
P3HT:O-IDTBR	59.52	CB+bromoanisole	5 [S15]
SMD2:ITIC	80	CB	5.25 [S31]
PBTIBDTT:ITIC-F	3.48	CB	8.6 [S27]
PBDB-T:ITIC	15	CB	8.9 [S30]
PTB7-Th:**T2-ORH**:EH-IDTBR	13.5	CF	10.08 [S28]

[a] CB = chlorobenzene, DCB = o-dichlorobenzene, and CF = chloroform

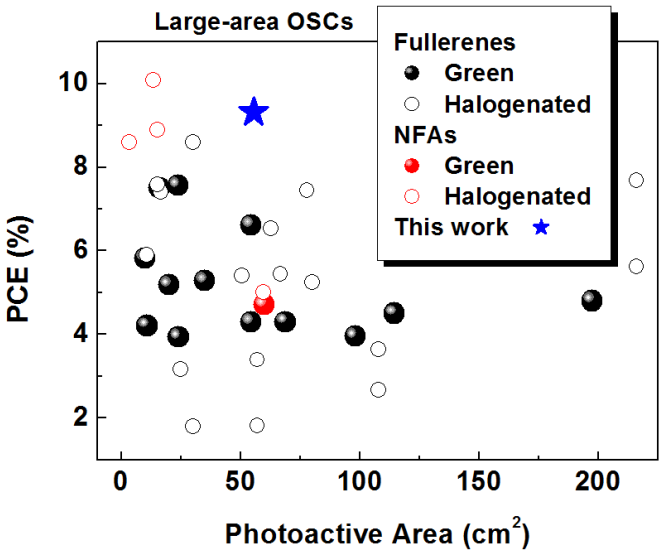

Figure S23. PCE versus photoactive area for large-area OSC modules

5. Characterization of the Binary OSCs

The binary OSCs were fabricated with the following inverted structure: ITO/ZnO NPs/PEIE/PTB7-Th:NFA/MoO_x/Ag (Table S6 and Fig S24). The best PCE of 9.28% was achieved with the PTB7-Th:**T2-OEHRH** dissolved in CF solution, with a J_{SC} value of 14.25 mA cm^{-2}, a V_{OC} value of 1.07 V and a *FF* of 61%, whereas the **T2-ORH**-based binary OSCs exhibited a PCE of 9.25% with a J_{SC} value of 14.52 mA cm^{-2}, a V_{OC} value of 1.08 V, and a *FF* of 59%. More surprisingly, the toluene-processed binary device with **T2-OEHRH** showed an impressive PCE of 9.70%, with a V_{OC} of 1.07 V, a J_{SC} of 14.57 mA cm^{-2}, and a *FF* of 62 %, which is an improvement even when compared with the PCE of its counterpart processed with CF solvent (9.28%). On the other hand, **T2-ORH**–based binary OSCs processed by toluene exhibited a poor PCE of 1.43% with V_{OC} of 0.40 V, *FF* of 32% and J_{SC} of 11.20 mA cm^{-2}. In addition, the binary OSCs based on PTB7-Th:EH-IDTBR processed with CF and toluene solvents exhibited the similar photovoltaic performances. The PCE of CF-processed PTB7-Th:EH-IDTBR OSC reached 9.58%, demonstrating an V_{OC} of 1.01 V, a J_{SC} of 15.21 mA cm^{-2} and a *FF* of 62 %, while the device processed with toluene attained a PCE of 10.05% with a V_{OC} of 1.02 V, a J_{SC} of 15.63 mA cm^{-2} and a *FF* of 63%. For large-area binary OSCs, the superior PCE can be achieved in **T2-OEHRH**-based devices as a best PCE of 6.20% (substrate size = 100 cm^2, aperture size = 55.5 cm^2) processed with the toluene solvent under ambient conditions using a D-bar coater (Table S6 and Fig S24b). Asymmetric **T2-OEHRH** exhibits the superior solubility and favorable morphology, which can effectively suppress excessive self-aggregation/crystallization as compared with the symmetric **T2-ORH**-based photoactive films. The correlation between the chemical structure and morphological behavior could be more precisely understood from the optical microscopy (OM) analysis. In OM images, the small-area photoactive films based on **T2-OEHRH** processed with CF (Fig S25d) and toluene (Fig S25e) solvents showed pinhole-free and uniform phase morphology. However, the **T2-ORH**-based films processed with CF solvent exhibited small dark spots, which was related with accumulated **T2-ORH** aggregation (Fig S25a). Furthermore, the large-area device based on the asymmetric **T2-OEHRH** with toluene solvent exhibited structural homogeneity and uniform morphology ascribed to the superior solubility (Fig S25f), whereas the counterpart **T2-ORH** device showed large rectangular-shaped domains attributed to strongly aggregated **T2-ORH** due to its poor solubility (Fig S25c). As a result, the asymmetric alkyl side-chain on NFA appears to be beneficial for application with small and large-area devices processed with the eco-friendly solvents.

Table S6. Summary of the optimized photovoltaic performances in binary-blend NFA-OSCs under simulated 1 sun (100 mW cm^{-2}, AM 1.5G) irradiation[a]

NFA	Solvent[b]	Aperture Size [cm^2]	V_{OC} [V]	J_{SC} [mA cm^{-2}]	*FF* [%]	PCE [%]
T2-ORH	CF	0.09[c]	1.08 (1.06±0.02)[e]	14.52 (14.38±0.13)[e]	59 (58±1)[e]	9.25 (8.99±0.25)[e]
	Toluene	0.09[c]	0.40 (0.37±0.04)[e]	11.20 (10.78±0.45)[e]	32 (28±5)[e]	1.43 (0.88±0.60)[e]
		55.5[d]	3.77 (3.28±0.50)[e]	0.71 (0.62±0.09)[e]	29 (25±4)[e]	0.79 (0.21±0.59)[e]
T2-OEHRH	CF	0.09[c]	1.07 (1.06±0.01)[e]	14.25 (14.09±0.15)[e]	61 (60±1)[e]	9.28 (9.03±0.26)[e]
	Toluene	0.09[c]	1.07 (1.06±0.01)[e]	14.57 (14.38±0.17)[e]	62 (62±1)[e]	9.70 (9.55±0.16)[e]
		55.5[d]	11.35 (11.04±0.21)	1.03 (1.00±0.03)[e]	53 (51±3)[e]	6.20 (5.98±0.21)[e]
EH-IDTBR	CF	0.09[c]	1.01 (1.00±0.02)[e]	15.21 (15.03±0.18)[e]	62 (61±1)[e]	9.58 (9.34±0.23)[e]
	Toluene	0.09[c]	1.02 (1.01±0.01)[e]	15.63 (15.39±0.25)[e]	63 (62±1)[e]	10.05 (9.78±0.27)[e]

[a] Inverted device architecture is ITO/ZnO NPs/PEIE/PTB7-Th:NFA = 1:2 (d = ~100 nm)/MoO_x/Ag. [b] Solvent additive treatment with 1.0 vol% DPE. [c] Photoactive layers are deposited by spin-casting in a globe box. [d] Photoactive films are deposited from bar coating method in air. [e] The average values with standard deviations in the brackets are obtained from over 5 independent devices.

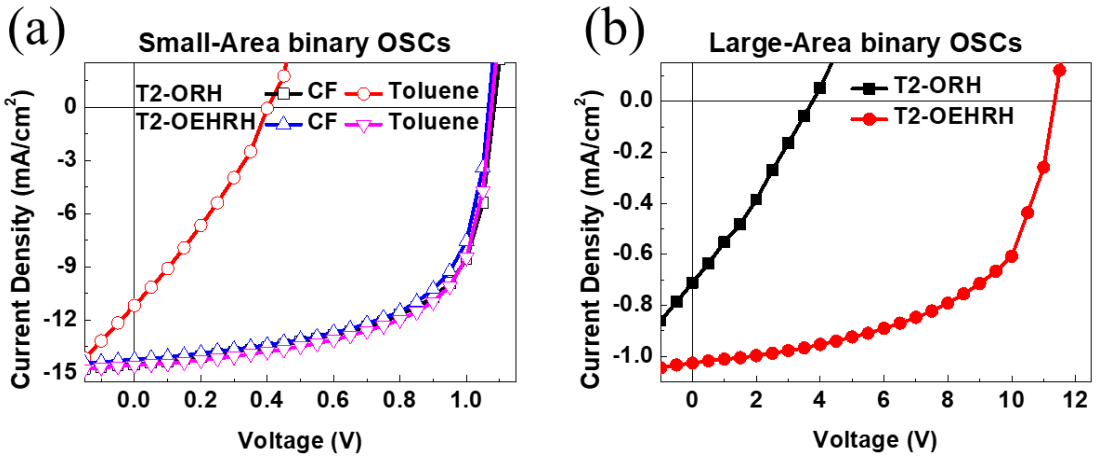

Fig S24. *J–V* curves of (a) small-area (aperture size = 0.09 cm^2) PTB7-Th:NFA binary OSCs processed with CF and toluene and (b) large-area (aperture size = 55.5 cm^2) binary OSCs processed with toluene solvent under ambient conditions using a D-bar coater.

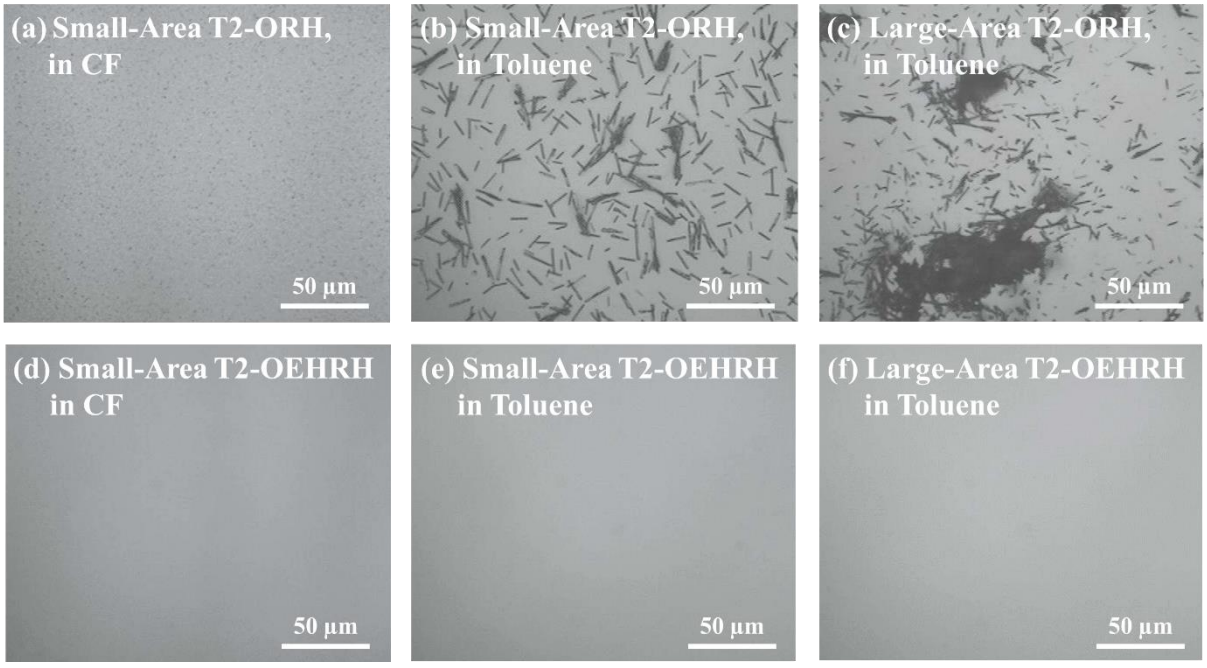

Fig S25. Optical microscopy images of small-area PTB7-Th:**T2-ORH** films with (a) CF and (b) toluene solvent processed from the spin-casting process, (c) large-area PTB7-Th:**T2-ORH** with toluene solvent processed from the D-bar coating process, small-area PTB7-Th:**T2-OEHRH** with (d) CF and (e) toluene solvent, and (f) large-area PTB7-Th:**T2-OEHRH** with toluene solvent.

6. References

[S1] a) Z. B. Henson, G. C. Welch, T. van der Poll, G. C. Bazan, *J. Am. Chem. Soc.* **2012**, *134*, 3766−3779; b) Q. V. Hong, C. E. Song, S.-J. Moon, S. K. Lee, J.-C. Lee, B. J. Kim, W. S. Shin, *Macromolecules* **2015**, *48*, 3918−3927

[S2] M. J. Frisch, G. W. Trucks, H. B. Schlegel, G. E. Scuseria, M. A. Robb, J. R. Cheeseman, G. Scalmani, V. Barone, B. Mennucci, G. A. Petersson, et al., Gaussian 16, Gaussian, Inc., Wallingford, CT, 2016.

[S3] O. Kwon, J. Jo, B. Walker, G. C. Bazan, J. H. Seo, *J. Mater. Chem. A* **2013**, *1*, 7118

[S4] a) D. Liu, B. Kan, X. Ke, N. Zheng, Z. Xie, D. Lu, Y. Liu, *Adv Energy Mater.* **2018**, *8*, 1801618; b) M. Zhang, Z. Xiao, W. Gao, Q. Liu, K. Jin, W. Wang, Y. Mi, Q. An, X. Ma, X. Liu, C. Yang, L. Ding, F. Zhang, *Adv Energy Mater.* **2018**, *8*, 1801968.

[S5] a) T. Daeneke, T.-H. Kwon, A. B. Holmes, N. W. Duffy, U. Bach, L. Spiccia, *Nat. Chem.* **2011**, *3*, 211-215; b) M. Quintana, T. Edvinsson, A. Hagfeldt, G. Boschloo, *J. Phys. Chem. C* **2007**, *111*, 1035–1041.

[S6] S.-L. Lim, K.-H. Ong, J. Li, L. Yang, Y.-F. Chang, H.-F. Meng, X. Wang, Z.-K. Chen, *Org. Electron.* **2017**, *43*, 55.

[S7] L. Lucera, F. Machui, P. Kubis, H. D. Schmidt, J. Adams, S. Strohm, T. Ahmad, K. Forberich, H. J. Egelhaaf, C. J. Brabec, *Energy Environ. Sci.* **2016**, *9*, 89.

[S8] Y. Q. Wong, H.-F. Meng, H. Y. Wong, C. S. Tan, C.-Y. Wu, P.-T. Tsai, C.-Y. Chang, S.-F. Horng, H.-W. Zan, *Org. Electron.* **2017**, *43*, 196.

[S9] S. Rasool, D. V. Vu, C. E. Song, H. K. Lee, S. K. Lee, J.-C. Lee, S.-J. Moon, W. S. Shin, *Adv. Energy Mater.* **2019**, *9*, 1900168.

[S10] L. Lucera, F. Machui, H. D. Schmidt, T. Ahmad, P. Kubis, S. Strohm, J. Hepp, A. Vetter, H. J. Egelhaaf, C. J. Brabec, *Org. Electron.* **2017**, *45*, 209

[S11] S. Berny, N. Blouin, A. Distler, H.-J. Egelhaaf, M. Krompiec, A. Lohr, O. R. Lozman, G. E. Morse, L. Nanson, A. Pron, T. Sauermann, N. Seidler, S. Tierney, P. Tiwana, M. Wagner, H. Wilson, *Adv. Sci.* **2016**, *3*, 1500342.

[S12] J. Zhang, Y. Zhao, J. Fang, L. Yuan, B. Xia, G. Wang, Z. Wang, Y. Zhang, W. Ma, W. Yan, W. Su, Z. Wei, *Small* **2017**, *13*, 1700388.

[S13] K. Zhang, Z. Chen, A. Armin, S. Dong, R. Xia, H.-L. Yip, S. Shoaee, F. Huang, Y. Cao, *Solar RRL* **2018**, *2*, 1700169.

[S14] Y.-M. Chang, C.-Y. Liao, C.-C. Lee, S.-Y. Lin, N.-W. Teng, P. Huei-Shuan Tan, *Sol. Energy Mater. Sol. Cells* **2019**, *202*, 110064.

[S15] S. Strohm, F. Machui, S. Langner, P. Kubis, N. Gasparini, M. Salvador, I. McCulloch, H. J. Egelhaaf, C. J. Brabec, *Energy Environ. Sci.* **2018**, *11*, 2225.

[S16] J. E. Lewis, E. Lafalce, P. Toglia, X. Jiang, *Sol. Energy Mater. Sol. Cells* **2011**, *95*, 2816.

[S17] P. Apilo, M. Välimäki, R. Po, K.-L. Väisänen, H. Richter, M. Ylikunnari, M. Vilkman, A. Bernardi, G. Corso, H. Hoppe, R. Roesch, R. Meitzner, U. S. Schubert, J. Hast, *Solar RRL*, **2018**, *2*, 1700160.

[S18] P.-T. Tsai, K.-C. Yu, C.-J. Chang, S.-F. Horng, H.-F. Meng, *Org. Electron.* **2015**, *22*, 166.

[S19] H. Jin, C. Tao, M. Velusamy, M. Aljada, Y. Zhang, M. Hambsch, P. L. Burn, P. Meredith, *Adv. Mater.* **2012**, *24*, 2572.

[S20] N. Agrawal, M. Zubair Ansari, A. Majumdar, R. Gahlot, N. Khare, *Sol. Energy Mater. Sol. Cells* **2016**, *157*, 960.

[S21] G. P. Kini, S. K. Lee, W. S. Shin, S.-J. Moon, C. E. Song, J.-C. Lee, *J. Mater. Chem. A* **2016**, *4*, 18585.

[S22] K.-M. Huang, Y. Q. Wong, M.-C. Lin, C.-H. Chen, C.-H. Liao, J.-Y. Chen, Y.-H. Huang, Y.-F. Chang, P.-T. Tsai, S.-H. Chen, C.-T. Liao, Y.-C. Lee, L. Hong, C.-Y. Chang, H.-F. Meng, Z. Ge, H.-W. Zan, S.-F. Horng, Y.-C. Chao, H. Y. Wong, *Prog. Photovolt: Res. Appl.* **2019**, *27*, 264.

[S23] T. T. T. Bui, M. Jahandar, C. E. Song, Q. V. Hoang, J.-C. Lee, S. K. Lee, I.-N. Kang, S.-J. Moon, W. S. Shin, *Sol. Energy Mater. Sol. Cells* **2015**, *134*, 148.

[S24] S. Hong, H. Kang, G. Kim, S. Lee, S. Kim, J.-H. Lee, J. Lee, M. Yi, J. Kim, H. Back, J.-R. Kim, K. Lee, *Nat. Commun.* **2016**, *7*, 10279.

[S25] S. Badgujar, G.-Y. Lee, T. Park, C. E. Song, S. Park, S. Oh, W. S. Shin, S.-J. Moon, J.-C. Lee, S. K. Lee, *Adv. Energy Mater.* **2016**, 1600228.

[S26] K.-M. Huang, C.-M. Lin, S.-H. Chen, C.-S. Li, C.-H. Hu, Y. Zhang, H.-F. Meng, C.-Y. Chang, Y.-C. Chao, H.-W. Zan, L. Huo, P. Yu, *Solar RRL* **2019**, *3*, 1900071.

[S27] T. Zhang, G. Zeng, F. Ye, X. Zhao, X. Yang, *Adv. Energy Mater.* **2018**, *8*, 1801387.

[S28] S. Oh, C. E. Song, T. Lee, A. Cho, H. K. Lee, J.-C. Lee, S.-J. Moon, E. Lim, S. K. Lee, W. S. Shin, *J. Mater. Chem.* A **2019**, 7, 22044.

[S29] J. Lee, Y.-H. Seo, S.-N. Kwon, D.-H. Kim, S. Jang, H. Jung, Y. Lee, H. Weerasinghe, T. Kim, J. Y. Kim, D. Vak, S.-I Na, *Adv. Energy Mater*. **2019**, 1901805.

[S30] X. Meng, L. Zhang, Y. Xie, X. Hu, Z. Xing, Z. Huang, C. Liu, L. Tan, W. Zhou, Y. Sun, W. Ma, Y. Chen, *Adv. Mater.* **2019**, 1903649.

[S31] Y. W. Han, S. J. Jeon, H. S. Lee, H. Park, K. S. Kim, H.-W. Lee, D. K. Moon, *Adv. Energy Mater*. **2019**, 1902065.